Femtosecond X-ray Diffraction of Laser-shocked Forsterite (Mg_2SiO_4) to 122 GPa

Donghoon Kim[1], Sally J. Tracy[1,2], Raymond F. Smith[3], Arianna E. Gleason[4], Cindy A. Bolme[5], Vitali B. Prakapenka[6], Karen Appel[7], Sergio Speziale[8], June K. Wicks[1,9], Eleanor J. Berryman[1,10], Sirus K. Han[1], Markus O. Schoelmerich[8], Hae Ja Lee[11], Bob Nagler[11], Eric F. Cunningham[11], Minta C. Akin[3], Paul D. Asimow[12], Jon H. Eggert[3], and Thomas S. Duffy[1]

[1]Department of Geosciences, Princeton University, Princeton, NJ, USA
[2]Now at Geophysical Laboratory, Carnegie Institution for Washington, Washington, DC, USA
[3]Lawrence Livermore National Laboratory, Livermore, CA, USA
[4]Fundamental Physics Directorate, SLAC, Menlo Park, CA, USA
[5]Shock and Detonation Physics, Los Alamos National Laboratory, Los Alamos, NM, USA
[6]Center for Advanced Radiation Sources, University of Chicago, Chicago, IL, USA
[7]European XFEL, Holzkoppel 4, Schenefeld, Germany
[8]GFZ German Research Centre for Geosciences, Telegrafenberg, Potsdam, Germany
[9]Now at Department of Earth & Planetary Sciences, Johns Hopkins University, Baltimore, MD, USA
[10]Now at CanmetMINING, Natural Resources Canada, Ottawa, ON, Canada
[11]Linac Coherent Light Source, SLAC National Accelerator Laboratory, Menlo Park, CA, USA
[12]Division of Geological and Planetary Sciences, California Institute of Technology, Pasadena, CA,USA

Corresponding author: Donghoon Kim (donghoon@princeton.edu)

Key Points:

- The atomic-level structure of forsterite under shock compression has been determined from 19 to 122 GPa.
- At shock stresses between 33 and 75 GPa, forsterite coexists with the metastable phase forsterite III along the Hugoniot.
- Above 79 GPa, polycrystalline forsterite undergoes amorphization while single crystals exhibit variable behavior depending on orientation.

Abstract

The behavior of forsterite, Mg_2SiO_4, under dynamic compression is of fundamental importance for understanding its phase transformations and high-pressure behavior. Here, we have carried out an *in situ* X-ray diffraction study of laser-shocked poly- and single-crystal forsterite (*a*-, *b*-, and *c*- orientations) from 19 to 122 GPa using the Matter in Extreme Conditions end-station of the Linac Coherent Light Source. Under laser-based shock loading, forsterite does not transform to the high-pressure equilibrium assemblage of $MgSiO_3$ bridgmanite and MgO periclase, as was suggested previously. Instead, we observe forsterite and forsterite III, a metastable polymorph of Mg_2SiO_4, coexisting in a mixed-phase region from 33 to 75 GPa for both polycrystalline and single-crystal samples. Densities inferred from X-ray diffraction data are consistent with earlier gas-gun shock data. At higher stress, the behavior observed is sample-dependent. Polycrystalline samples undergo amorphization above 79 GPa. For [010]- and [001]-oriented crystals, a mixture of crystalline and amorphous material is observed to 108 GPa, whereas the [100]-oriented crystal adopts an unknown crystal structure at 122 GPa. The Q values of the first two sharp diffraction peaks of amorphous Mg_2SiO_4 show a similar trend with compression as those observed for $MgSiO_3$ glass in both recent static and laser-compression experiments. Upon release to ambient pressure, all samples retain or revert to forsterite with evidence for amorphous material also present in some cases. This study demonstrates the utility of femtosecond free-electron laser X-ray sources for probing the time evolution of high-pressure silicates through the nanosecond-scale events of shock compression and release.

1. Introduction

Mg-rich olivine, $(Mg,Fe)_2SiO_4$, occurs widely in igneous and metamorphic rocks, and is the dominant phase in Earth's upper mantle (Ringwood, 1991). The physical properties of amorphous and liquid Mg_2SiO_4 are also important for modeling partial melting of the mantle and the behavior of magma oceans (Mosenfelder et al., 2007). In addition, olivine is a common constituent of terrestrial planets (Mustard et al., 2005) and meteorites (Mason, 1963), and is also found in comets (Hanner, 1999), pre-solar grains (Nguyen, 2004), and in accretion disks around young stars (van Boekel et al., 2004).

Static compression experiments have shown that at high pressure and temperature (>1000 K), $(Mg,Fe)_2SiO_4$ adopts a spinelloid structure (wadsleyite) at about ~14 GPa, and then transforms to a spinel structure (ringwoodite) at ~18 GPa (Frost, 2008). At 24 GPa, ringwoodite dissociates into $(Mg,Fe)SiO_3$ bridgmanite and (Mg,Fe)O, which are expected to be the major phases of Earth's lower mantle. These phase transitions in olivine and its polymorphs are the primary cause of the major seismic discontinuities at 410-, 520-, and 660-km depths in the Earth's mantle (Ringwood, 1991). These discontinuities play a key role in controlling the dynamics and heat flow in the Earth's interior (Ringwood, 1991).

Metastable polymorphs of Mg_2SiO_4, the Mg end-member of olivine, have also been reported at high pressure. A 300-K single-crystal X-ray diffraction (XRD) study showed that forsterite (orthorhombic space group *Pbnm*) transforms to forsterite II (triclinic, *P*1) and forsterite III (orthorhombic, $Cmc2_1$) at 50 and 58 GPa, respectively (Finkelstein et al., 2014) (hereafter Fo, Fo II, and Fo III, respectively). Fo III is related to the post-spinel calcium titanate structure and has fully 6-coordinated silicon. It remains metastable to at least 160 GPa at ambient temperature (Lavina, 2019).

Due to the geophysical importance of Mg-rich olivine, there has been much interest in understanding its shock-compression behavior (e.g., Brown et al., 1987; Furnish and Brown, 1986; Jackson and Ahrens, 1979; Jeanloz, 1980; Langenhorst et al., 1999; Mosenfelder et al., 2007; Newman et al., 2018; Syono et al., 1981a; Watt and Ahrens, 1983). The Hugoniot of forsterite has been interpreted to reflect transformation to a high-pressure phase through a broad mixed-phase region that begins at about 50 GPa and is completed near 100 GPa (Mosenfelder et al., 2007). This stress is much greater than that required for transformation of olivine in static experiments, suggesting that the role of kinetics is captured on the short timescales of shock experiments. The metastable Fo III phase has been reported in recent gas-gun experiments at 44 and 73 GPa based on *in situ* XRD data (Newman et al., 2018). However, the exact natures of the mixed-phase and high-pressure phase regions are still not well understood. Upon shock compression to higher pressure, olivine is reported to melt at ~150 GPa on the Hugoniot (J. M. Brown et al., 1987).

The dynamic behavior of olivine is also of interest for understanding shock metamorphism generated by hypervelocity impacts on planetary bodies (Falko Langenhorst, 2002). High-pressure olivine polymorphs have been identified in shocked meteorites as a result of solid-solid phase transformations or crystallization of silicate liquids (Gillet et al., 2007). Ringwoodite, for example, has been identified in chondrites and Martian meteorites (Gillet et al., 2007). Analyses of such phases have been used to explore the shock and post-shock pressure-temperature history, as well as the dynamic deformation mechanisms. None of the laboratory-based shock-recovery experiments on olivine provide direct evidence for a phase transformation or disproportionation under shock compression (Bauer, 1979; Jeanloz, 1980; F. Langenhorst et al., 1999; Müller & Hornemann, 1969; Reimold & Stöffler, 1978; Shinno, 2002) with the exception of Syono et al. (1981). They reported evidence for $MgO + MgSiO_3$ glass in samples recovered from Fo shocked above 80 GPa.

Constraining the behavior of olivine under dynamic loading is necessary for understanding its metastable states, transformation pathways and kinetics, structural polymorphism, and equations of state, which all play a role in interpreting geophysical phenomena. Here, we report the results of *in situ* XRD measurements on laser-shock experiments on forsterite samples covering a wide pressure range.

2. Material and methods

2.1. Sample Preparation

Synthetic single-crystal and polycrystalline Fo (Mg_2SiO_4) samples were used in this study. The single-crystal samples (Roditi International, unit-cell volume V_0=290.0 Å^3) were cut into ~ 50-μm thick slices from a 10 x 10 x 10 mm^3 cube , with the main face of each slice oriented normal to the *a*-, *b*-, or *c*-axis. Sintered polycrystalline aggregates with negligible porosity, cut to the same dimensions, were also used. The polycrystalline samples were from the same sources as used in Newman et al. (2018). The approximate mean grain size was 10 μm and the measured unit-cell volume was 289.7 Å^3 with a corresponding density 3.225 g/cm^3.

2.2. Laser Shock Experimental Configuration

Laser-driven shock-compression experiments were performed at the Matter in Extreme Conditions (MEC) end-station of the Linac Coherent Light Source (LCLS) at the Stanford Linear Accelerator Center (SLAC) (Nagler et al., 2015). Target packages consisted of a 75-μm thick polyimide (CH) ablator glued to a Fo sample with or without a 100-μm (100) LiF window

epoxied to the rear surface (Figure 1). Epoxy layers were approximately 1-μm thick. The rear surface of the Fo was coated with a0.2-μm layer of Ti to enhance the reflectivity of the sample. A 0.2-μm Al coating was deposited on the ablation side of the CH to ensure that the laser drive was optimally coupled at this interface.

Samples were shock compressed using one or both of the lasers from a two-beam 527 nm Nd:glass laser system (S. B. Brown et al., 2017) (Fig. 1). The laser pulses were 10–15 ns in duration with a quasi-flat-top shape (Supplemental Material, Fig. S1). Experiments were performed both with and without phase plates. The shock stress was varied from 19 to 122 GPa by tuning the laser spot size (≤ 300 μm), pulse length (10–15 ns) and laser energy (≤ 60 J). Pulse shapes were monitored to assess the reproducibility of the drive conditions for a given laser energy, pulse length, and spot size (Supplemental Material, Table S1).

2.3. Pressure Determination

The forsterite free surface or Fo/LiF interface velocity was monitored by a line-imaging velocity interferometer system for any reflector (VISAR) with a 532-nm wavelength laser. Two independent VISAR channels with different velocity sensitivities were used to resolve ambiguities in velocity resulting from limitations in the time response of the system. The VISAR also provided information on the shock arrival time, spatial planarity, and peak elastic stress. For a given drive condition, the peak stress in a sample backed by a LiF window was determined by impedance matching using the measured interface particle velocity (u_P) and the known equations of state of Fo and LiF (Supplemental Material, Figs. S2-S3 and Table S2). As the strength of forsterite on the Hugoniot is poorly constrained, we have not made any correction for the difference between axial stress (P_X) and mean pressure (P). The error in pressure was determined from propagation of uncertainties in the impedance-matching analysis.

2.4. *In-situ* X-ray Diffraction Analysis

Samples were probed by angle-dispersive X-ray diffraction. The LCLS provided quasi-monochromatic ($\Delta E/E$ = 0.2-0.5%), 8.5 keV, X-ray pulses of 60-fs duration, each containing 10^{12} photons. The X-rays were incident to 30° relative to target normal and focused to a spot size of ~20 μm at the center of the laser drive. Diffraction peaks from the sample were recorded on four Cornell-SLAC Pixel Array Detectors (CSPAD 550k) (Philipp et al., 2011), covering a two-theta, 2θ, range of 15-85° (Supplementary Material, Fig. S4). For each shot, we also collected one or more pre-shot XRD patterns with the incident X-ray intensity attenuated by 30-90%. This provided a pre-compression reference pattern and facilitated screening for strong single-crystal diffraction spots that could damage the detector. The two-dimensional (2D) CSPAD images were integrated azimuthally to convert them to one-dimensional (1D) XRD patterns. The intensity of the integrated pattern corresponding to each CSPAD was adjusted by equalizing the background from each detector. CeO_2 and LaB_6 were used as standards to calibrate the sample-to-detector distance and the orientation of each detector using the program Dioptas (Prescher & Prakapenka, 2015).

A time series of diffraction patterns was collected by changing the XRD probe time on a sequence of shots using the same drive conditions and nominally identical targets with and without a LiF window. The stress for the series of shots was determined from the target with a LiF window. The shock-arrival time at the LiF window or the free surface was designated as t = 0. XRD patterns record both the compressed material and uncompressed material ahead of the shock front at time points before the shock wave reaches the LiF window or free surface ($t < 0$).

In contrast, XRD patterns collected at $t > 0$ include a combination of compressed and partially released material. At time points late relative to shock propagation times, only diffraction from released materials is recorded.

Diffraction peak assignments were initially made by comparing the observed peaks to predicted peak positions based on 300-K static data (Finkelstein et al., 2014) at similar pressures. Lattice *d*-spacings were obtained by peak fitting, and unit-cell parameters were refined by least-squares fitting (Supplemental material, Table S3 and S4). It should be noted that some shots record only a few diffraction peaks, potentially limiting the precision of the unit-cell determination.

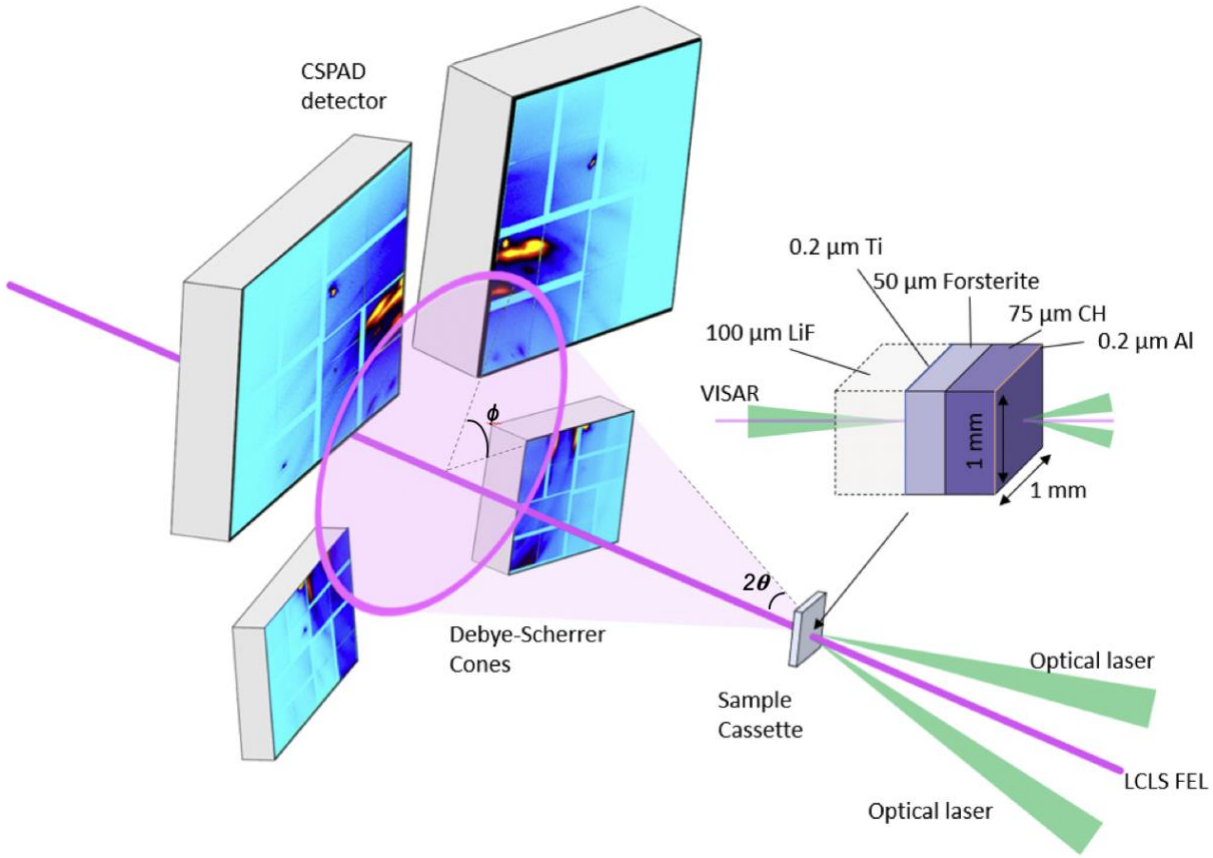

Figure 1. Schematic of the experimental setup for X-ray diffraction under laser-driven shock compression. The target package consisted of a CH ablator and a forsterite sample (with or without a LiF window). Diffraction was recorded on four CSPAD detectors. The VISAR laser was directed normal to the rear surface of the target to measure either the Fo-LiF-interface particle velocity or the free-surface velocity.

3. Results

Experiments were conducted at stresses from 19-122 GPa. Over this range, the shock-transit time for the 50-µm thick Fo sample was ~7-4.5 ns. Figure 2 shows the determined stresses

and calculated temperatures along with the equilibrium phase boundaries and 300-K metastable phases for Mg_2SiO_4 (Fig. 2). The peak stress achieved for each sample type is listed in the Supplemental Material, Table S1.

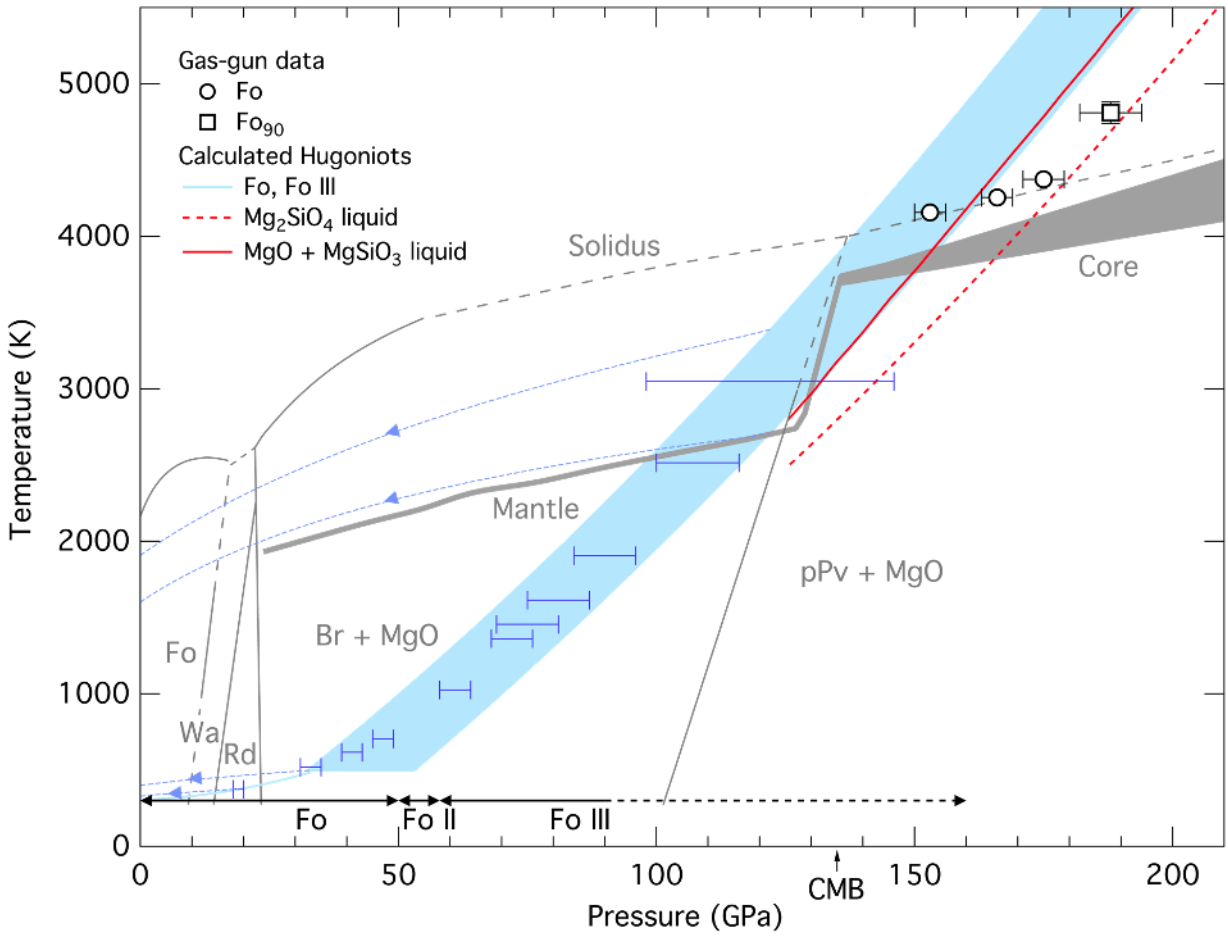

Figure 2. Phase diagram for Mg_2SiO_4 together with 300-K metastable phases (Fo II and Fo III; Finkelstein et al., 2014). Estimated Hugoniot pressure-temperature states (blue shaded region) for forsterite and Fo III were calculated using the thermodynamic parameters listed in the Supplemental Material, Table S6. The stresses (with uncertainty) for the present study are shown as blue lines. The light-blue dashed curves show calculated release isentropes, assuming no phase changes occur upon release. Measured temperatures for forsterite and olivine (Fo_{90}) shock-compressed in gas-gun experiments (Luo et al., 2004) are shown as open circles and a square, respectively. The gray band shows a representative geotherm for the Earth. Abbreviations used are: Fo – forsterite, Wa – wadsleyite, Rd – ringwoodite, Fo II – forsterite II, Fo III – forsterite III, Br – bridgmanite, pPv – post-perovskite, CMB – the core-mantle boundary. Sources are: Mg_2SiO_4 phase diagram (Katsura & Ito, 1989; Luo et al., 2004; Oganov & Ono, 2004; Zerr, 1998), geotherm (Stacey & Davis, 2008; Tateno et al., 2010), calculated Hugoniot curves (red solid and dashed lines) (de Koker et al., 2008).

3.1. Low-Pressure Phase Regime (up to ~ 25 GPa)

Compressed forsterite was identified in XRD patterns collected from single crystals shocked to 19 ± 1 GPa and 25 ± 1 GPa. Figure 3a shows a time series of XRD patterns for the [100]-single-crystal sample at ~ 19 GPa. Prior to the shot, we observe only diffraction from the (211) peak and, in some cases, 1-2 other single-crystal peaks. Upon compression, the (211) peak is shifted to higher two-theta values, and a few additional compressed forsterite diffraction spots are observed, likely due to the single crystal breaking into a few crystallites (Fig. S5). This is consistent with laboratory-based recovery experiments that report compressional fracture as a dominant deformation mechanism at these stresses (Bauer, 1979). Elongation of the spots in the azimuthal direction may reflect an increase in the mosaicity of the crystallites. There is no evidence of a phase transition at 19 GPa, consistent with gas-gun wave-profile measurements (M. D. Furnish et al., 1986). At +1.3 and +6.1 ns, the observed peaks shift to lower two-theta angles, indicating that release waves have reduced the stress. By +23.1 ns, diffraction spots, now frequently elongated along two-theta, are observed for multiple peaks that are all consistent with forsterite (Figs. 3a and S5). The increased number of observed diffraction spots indicates that the crystallite size is reduced, and their orientation distribution broadens especially at late times during the unloading process, likely due to fracturing resulting from interactions among unloading waves.

3.2. Mixed-Phase Regime (33 GPa – 75 GPa)

Figure 3b shows a time series of XRD patterns for forsterite shocked to a stress of 33 ± 2 GPa. Here the diffraction peaks show evidence for further fracturing and lattice strain in the crystallites (Fig. S5). In addition, the observed peaks at -1.5 ns can no longer be solely assigned to forsterite. In particular, new peaks appear near a two-theta value of 34° and between 42- 47°. We attempted to index the new peaks using the structural parameters of known high-pressure polymorphs of Mg_2SiO_4 (Smyth et al., 2000a, 2000b). Diffraction from wadsleyite, ringwoodite, or a mixture of bridgmanite and periclase cannot explain the observed patterns. Instead, we find that the metastable phases Fo II and Fo III (Finkelstein et al., 2014) can provide a reasonable match (Fig. 3b). It should be noted that Fo II crystallizes in the triclinic system ($P1$, Z=4) resulting in a complex diffraction pattern with many reflections. The large grain size maintained above the phase transition gives rise to insufficient powder averaging and diffraction spots to identify phases. This makes it difficult to rule out Fo II as a candidate phase. For simplicity, we have assigned the new peaks as Fo III throughout. Fo II and Fo III are both members of the post-spinel family of AB_2X_4 compounds. Ab initio calculations suggest that only Fo III is expected to be dynamically metastable (Bouibes & Zaoui, 2020; Zhang et al., 2019).

Our results are in agreement with recent *in situ* XRD results from gas-gun experiments, which first reported evidence for the formation of Fo III during dynamic loading of forsterite (Newman et al., 2018). We observe Fo III at a lower stress (~33 GPa) than reported observations of 50 and 58 GPa in 300-K static-compression experiments (Finkelstein et al., 2014) and 44 GPa in gas-gun experiments (Newman et al., 2018). Notably, *ab initio* computational studies have indicated that metastable Fo III may be able to form at as low as ~22 GPa (Zhang et al., 2019). These results show that the transformation from Fo to Fo III can proceed readily over timescales ranging from 10 ns (this study) to hundreds of ns (gas gun) as well as under 300-K static compression.

Shortly after the beginning of release (+2.0 ns), Fo III peaks are still observed, but are markedly weaker (Fig. 3b). Based on the measured unit-cell volume (V = 264 $Å_3$) of forsterite,

the estimated stress at this time point is near 15 GPa. Fo III is retained until 12 GPa on decompression at 300 K in diamond-anvil-cell experiments (Finkelstein et al., 2014). By +5.5 ns, the observed pattern can be indexed as forsterite except for a single peak near a two-theta value of 18°, which corresponds to the (002) reflection of Fo III. At +28.5 ns, all diffraction peaks can be assigned to Fo. The unit-cell volume (V = 300 Å$_3$) at this time is larger than that of ambient forsterite (V = 290 Å$_3$). In addition, a broad feature is observed over 20-30° two-theta (Fig. S5), suggesting the possible presence of amorphous material. In static experiments, the amorphization of Fo III at ambient conditions was observed on decompression below 12 GPa (Finkelstein et al., 2014).

Fo III peaks were observed for all four types of starting materials when shock-compressed to stresses in the range of 33 to 75 GPa (Supplemental Material, Table S1). In experiments on an [010]-oriented crystal shocked to 40 ± 2 GPa, a mixture of compressed Fo and Fo III was observed (Fig. S6). The lattice parameters of the Fo III could not be determined due to an insufficient number of observed peaks. Figure 4 shows the 2D diffraction image and corresponding integrated 1D pattern for [010] Fo shocked to 72 ± 4 GPa. The observed peaks are indexed as a mixture of Fo and Fo III. The integrated pattern is similar to that obtained from gas-gun shock-compression experiments (Newman et al., 2018) (Fig. S7). However, in contrast to Newman et al. (2018), who interpreted their gas-gun XRD pattern as a complete transformation to Fo III, our interpretation is that compressed Fo and Fo III coexist at 40-44 and 72-73 GPa under both laser and gas-gun compression (Fig. S7).

The 72-GPa diffraction pattern for shock-compressed [010] forsterite shows a complex combination of broad spots and ring-like peaks (Fig. 4). In this case, we observed that the single-crystal sample was altered by the X-ray beam during the pre-shot diffraction measurement. As shown in Fig. S8, exposure of single-crystal sample to the FEL X-ray beam resulted in the appearance of multiple diffraction spots on subsequent exposure. This indicated that the single crystal disintegrated into smaller crystallites. X-ray damage due to FEL pulses has been identified in previous studies on diamond and other materials (Inoue et al., 2016; Medvedev et al., 2018).

Figure 5 shows the relative lattice parameters determined for Fo and Fo III in this study compared with previous shock (gas-gun) and static-compression data (Supplemental Material, Table S1). Although there are considerable uncertainties in the shock-wave data due to the spotty nature of the patterns as well as stress uncertainty, the lattice parameters are generally consistent with static data (Finkelstein et al., 2014; Newman et al., 2018) and *ab initio* computations (Zhang et al., 2019). Shock-induced defects and shear stresses may account for discrepancies between our data and some *ab initio* studies (Zhang et al., 2019).

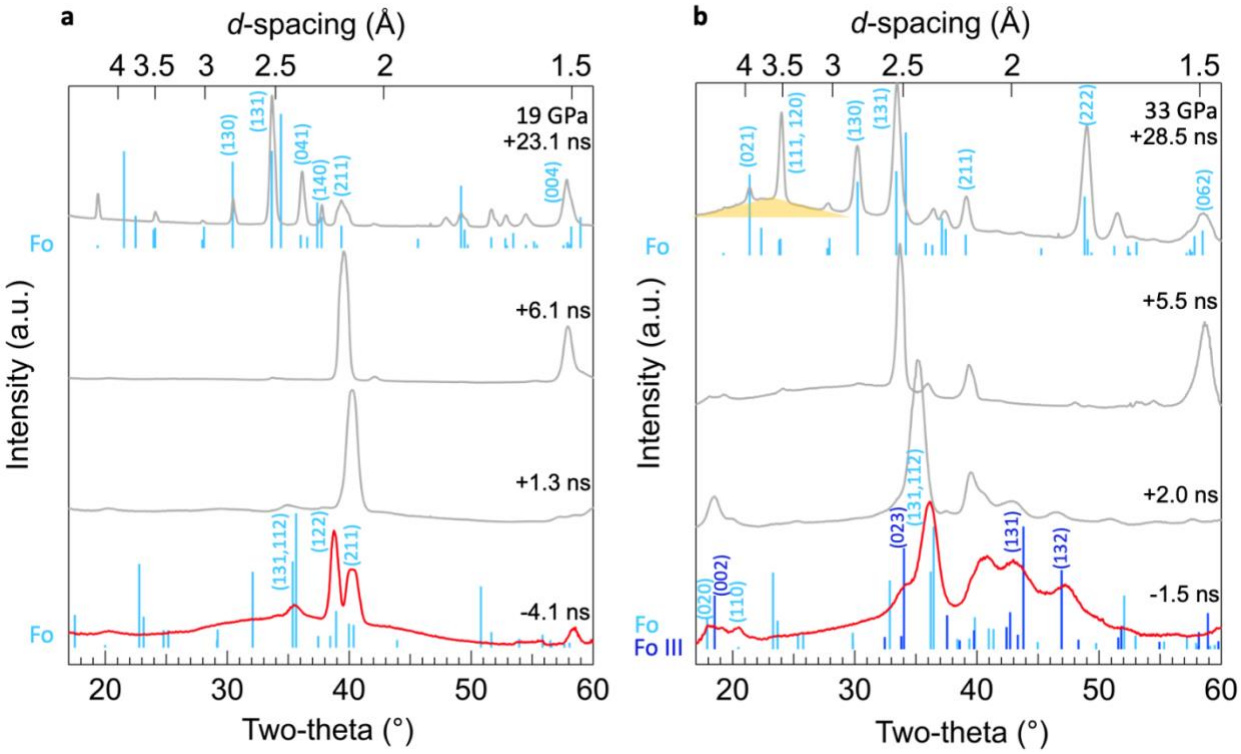

Figure 3. Integrated diffraction patterns for [100]-oriented single-crystal forsterite shots. X-ray probe times are with respect to the shock arrival at the LiF window or the free surface. **a**) At ~19 GPa, the pattern can be indexed as forsterite as indicated by the light blue tick marks below the pattern. **b**) At 33 GPa, Fo and Fo III peaks (blue tick marks) are observed at probe times of -1.5 to 2.0 ns. Upon decompression by +5.5 ns to 28.5 ns, only Fo peaks and amorphous structure (yellow shaded region) are observed.

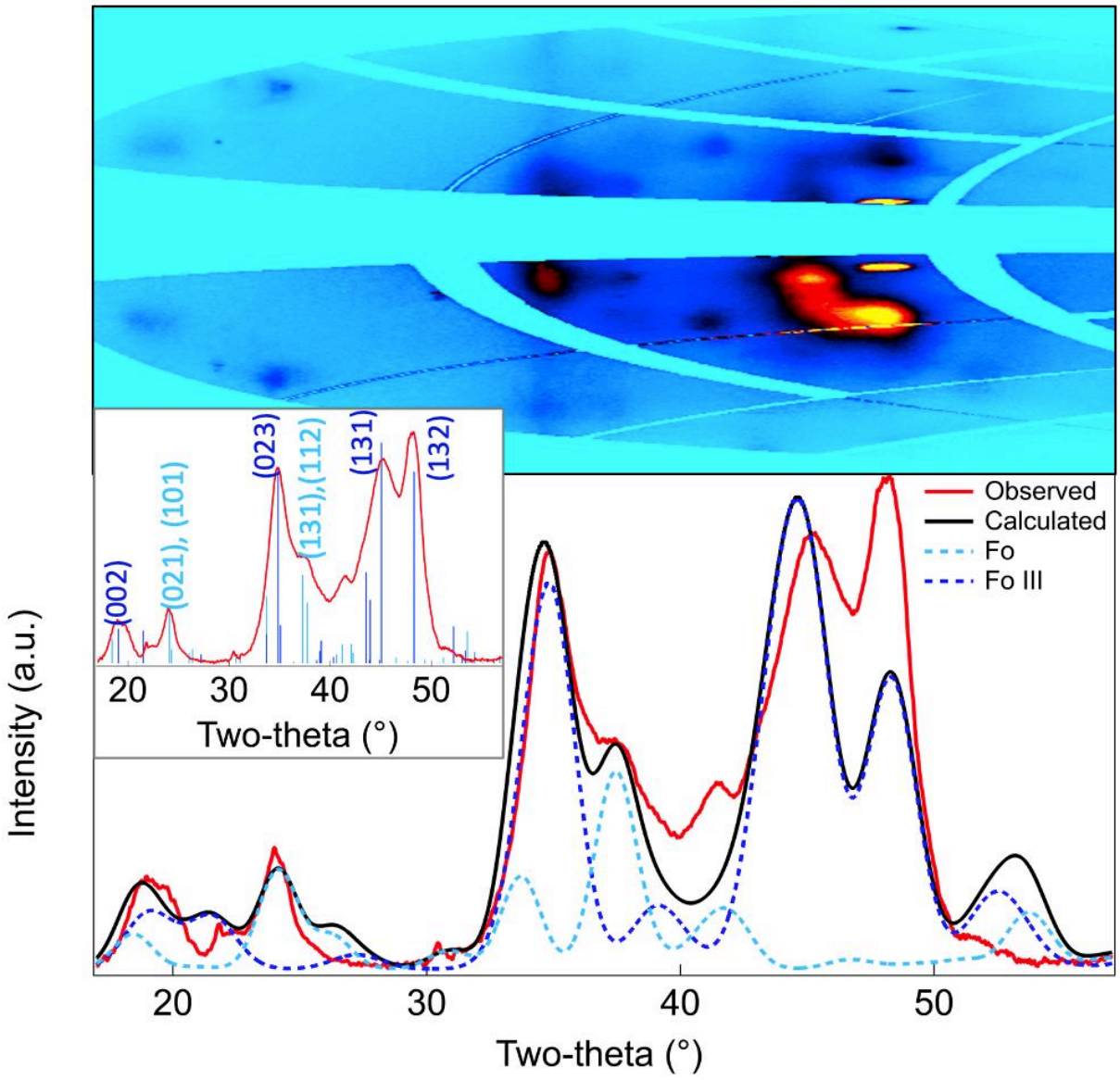

Figure 4. Background-subtracted 1D diffraction pattern (below) with CSPAD images (above) for [010]-oriented forsterite shocked to 72 GPa compared to the calculated pattern (black) for a mixture of forsterite (light blue, dashed) and Fo III (blue, dashed). The mixed phase assemblage can explain the observed peaks (inset) and largely matches the observed intensities.

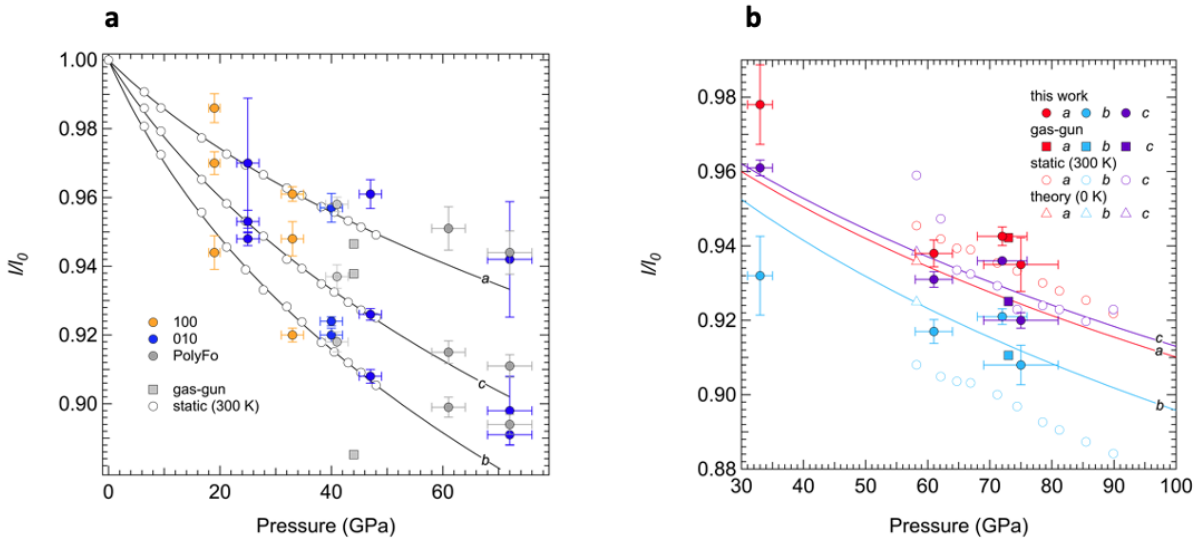

Figure 5. Relative unit-cell axial lengths of (**a**) forsterite and (**b**) Fo III under shock and static compression. **a**) Filled symbols are shock data (this study and gas-gun measurements (Newman et al., 2018)) and open symbols are static data (Finkelstein et al., 2014). The 300-K Fo pressure-volume equation of state (EOS) from static-compression data are shown as black solid lines. **b**) Open symbols are static (Finkelstein et al., 2014) and theoretical data (Zhang et al., 2019). The Fo III EOS from the theoretical data is shown as red, purple and light-blue solid lines. For tabular data, see the Supplemental Material, Table S1.

3.3. High-Pressure Phase Regime (above 79 GPa)

Although Fo III is observed at 61 ± 3 GPa for the shocked polycrystalline sample, the diffraction pattern changes between 79 ± 5 and 90 ± 6 GPa (Fig. 6a). At these stresses, we observe two broad, untextured peaks, which we interpret as amorphization of the sample (see discussion below). On release from these stresses, diffraction spots begin to emerge, indicating crystallization from the amorphous phase (top traces in Fig. 6a). Predicted diffraction peak positions for Fo III are compared to the observed pattern in Fig. S9, but neither Fo III nor Fo can explain one peak near a two-theta value of 41-42°. We speculate that a related post-spinel structure may form on release. A variety of related post-spinel structures have been identified in AB_2X_4 compounds at high pressure (Errandonea, 2014; Yamanaka et al., 2008).

Diffraction measurements were performed for the [010] and [001] orientations at 108 ± 8 GPa (Fig. 6b). In contrast to the polycrystalline material, these diffraction patterns show evidence of significant disordering, but not complete amorphization. The [001] sample retains a higher degree of crystallinity than the [010] orientation. Upon integration, the diffraction patterns for all three crystals are broadly similar, consisting of two broad diffraction features near 36 and 47° two-theta (Fig. 6b). This suggests that there is a continuous evolution from a disordered crystal to a fully amorphous phase with an amorphization stress that depends on the sample's starting orientation.

In contrast, [100] forsterite shocked to a peak stress of 122 ± 24 GPa retains a high degree of crystallinity as indicated by the spotty nature of the diffraction pattern (Fig. 6b). In this

case, the observed peaks cannot be indexed as Fo nor Fo III, as neither of these structures alone nor a mixture of the two phases can explain the peak near a two-theta of 44° (~1.95 Å) (Fig. 7). We attempted to index the peaks to other possible post-spinel-type phases of Mg_2SiO_4, but could not explain the observed peaks. High-pressure equilibrium phase assemblages such as bridgmanite and periclase or post-perovskite and periclase also fail to explain the observed pattern. Therefore, [100] Fo shocked to this stress appears to transform to an unknown high-pressure phase or a mixture of Fo III and an unknown phase.

Just after breakout (+0.2 ns), the diffraction peaks broaden (Figs. 7 and S5c). The two shots at the same delay time show different degrees of crystallinity, which may reflect shot-to-shot variation of the sample thickness, peak stress for a particular laser setting, or a heterogeneous stress state on release (Fig. S5).

Upon release at +5.2 ns, sharp Fo peaks are observed, demonstrating that this unknown phase or phase assemblage reverts to forsterite (V = 297~300 $Å_3$) on decompression (Fig. 7). This is consistent with our lower stress results. At +10.4 ns, two sets of closely spaced Fo diffraction peaks are observed, suggesting that the interaction of release waves produces a heterogeneous stress condition. Additionally, we observe a broad background at low two-theta, comparable to the Mg_2SiO_4 liquid and glass reported by Wilding et al. (2008). This suggests that the unknown phase may have become amorphous or could be partially melted due to the residual high temperature on release (Fig. 2).

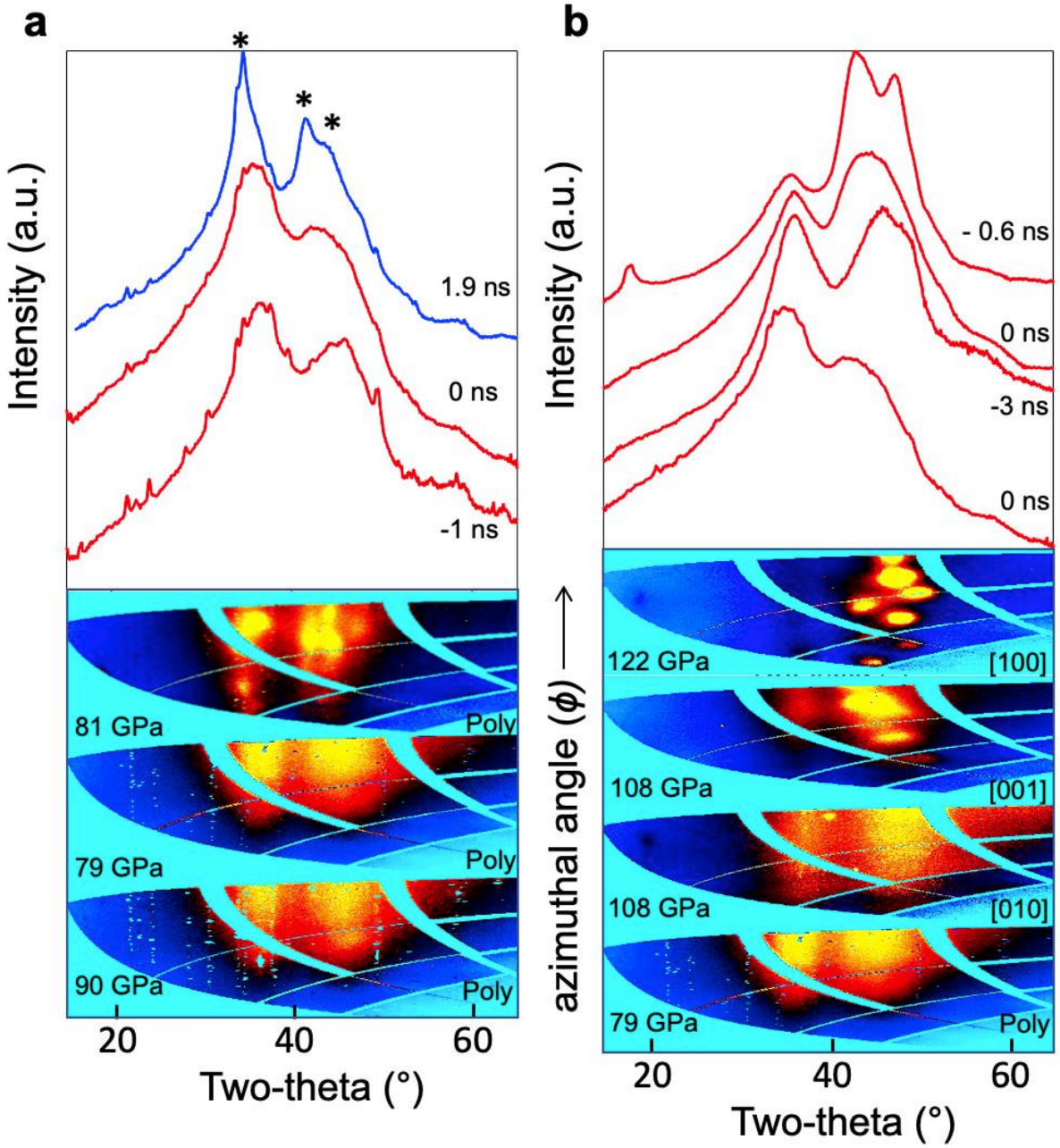

Figure 6. Integrated X-ray diffraction patterns compared with CSPAD images. **a**) Time series at a peak stress of 79 - 90 GPa for a polycrystalline sample. The sample becomes amorphous at these stresses on compression. Diffraction peaks from the uncompressed starting material produce the small, sharp peaks on the 79- and 90-GPa spectra. These peaks are mostly masked here to more clearly show the amorphous structure. Upon release (+1.9 ns), new peaks (asterisks) appear that cannot be assigned to forsterite or Fo III. **b**) The degree of amorphization is highly dependent on the starting material (see the lower CSPAD images). A fully amorphous structure is observed at 79 GPa for the polycrystalline sample, whereas a partial loss of crystallinity and amorphous structure are observed for the [010] and [001] samples at 108 GPa. The [100] sample retains crystalline peaks at 122 GPa.

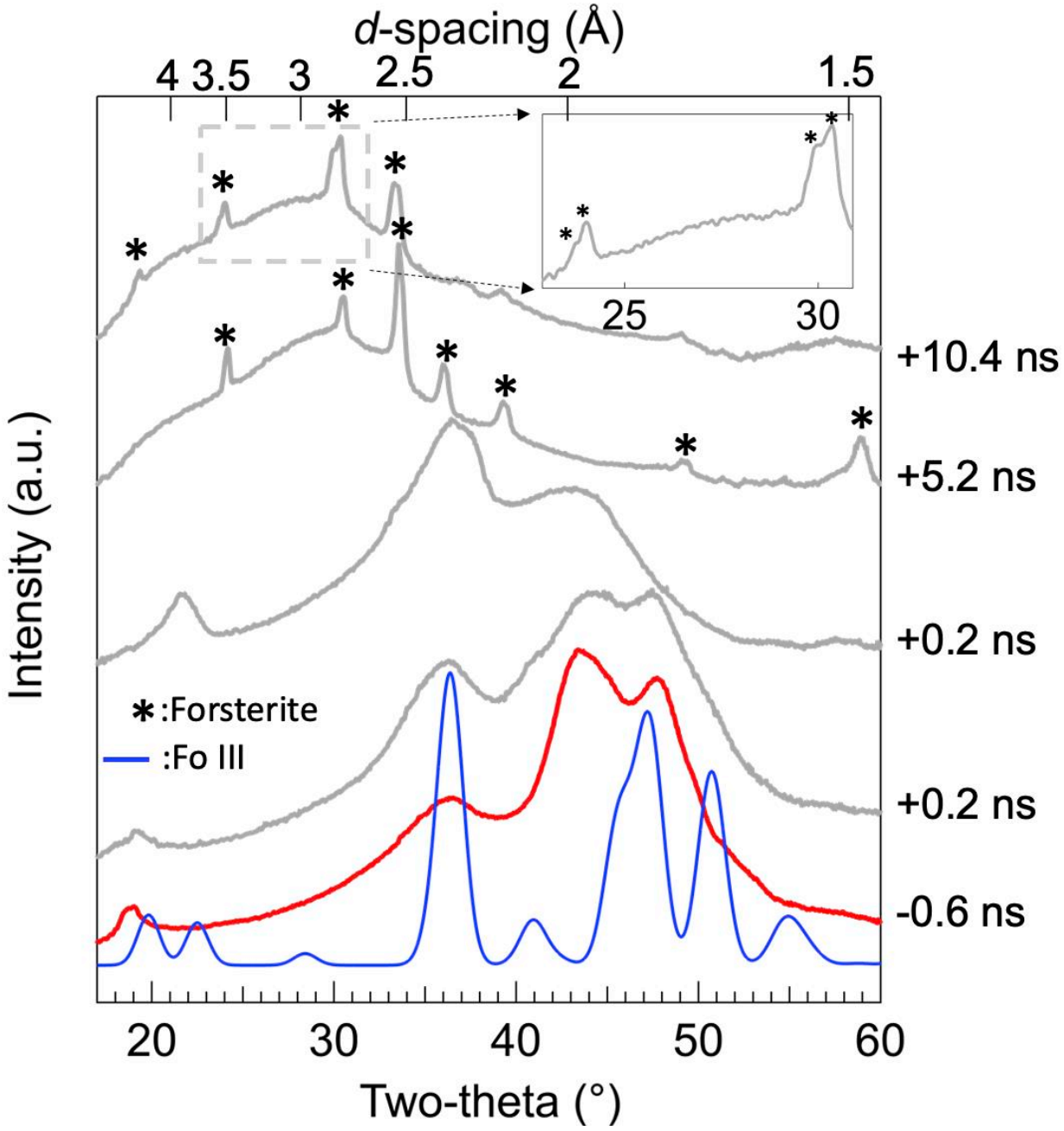

Figure 7. Integrated diffraction patterns for time series of shock compressed [100]-oriented forsterite collected at a peak stress of ~122 GPa for [100] single crystals. The calculated pattern for Fo III (blue) is compared to the observed data (red, gray). Asterisks indicate forsterite peaks upon release. The inset shows an expanded view of the region in the gray box.

4. Discussion

4.1. Wave profiles and peak elastic stress

The VISAR wave profiles provide constraints on the peak elastic precursor stress, σ_E, of forsterite under the nanosecond timescales of laser-shock compression. The highest-quality data were obtained for the [010]-oriented single-crystal starting material as shown in Fig. S10. The measured σ_E values are 13, 18 and 26 GPa for shots corresponding to peak sample stresses of 40, 47 and 72 GPa, respectively, using the orientation-dependent Us-u_P relation in the elastic region shown in Fig. S3 (Syono, Goto, Sato, et al., 1981). These values are larger than the previously reported σ_E of 12 GPa for crystals shocked along [010] to peak stresses of 15-37 GPa from gas-gun studies (Syono, Goto, Sato, et al., 1981). Our results show a strong correlation between σ_E and the peak stress, which was also not observed in the gas-gun experiments. A large increase in σ_E in high-strain-rate laser-driven compression experiments has also been reported in other materials (Smith et al., 2011; Tracy et al., 2019). None of the measured wave profiles show evidence for any additional multi-wave structure that could be associated with a crystalline phase transformation or amorphization.

4.2. Equation of state

A mixture of Fo and Fo III is observed on the Hugoniot from 33 to 75 GPa. Figure 8 shows densities obtained from our XRD measurements compared with those measured at the continuum level from gas-gun experiments. Beginning at 28 GPa, continuum Hugoniot states become at first slightly and then increasingly denser than forsterite at 300 K, consistent with the appearance and growth of the denser polymorph, as observed in our XRD data. Above 60 GPa, the densities of Fo III determined from our X-ray data are similar to static-compression results for this phase (Finkelstein et al., 2014). The fraction of Fo III is ~50-80 %, based on a comparison of the densities derived from the XRD patterns for Fo and Fo III at 72 GPa (Fig. 4) with those measured at the continuum level in gas-gun experiments at about this stress (Fig. 8). This is broadly comparable to the observed relative diffraction intensities of the spotty sample, although given the large crystal size only qualitative analysis of peak intensities is possible (Fig 4).

In light of these findings, we recalculated linear fits to the shock velocity – particle velocity relationships for forsterite from gas-gun experiments using our new assignments for the low-pressure phase (LPP) and mixed-phase (MP) regimes (Fig. S3). The best-fit relationships along the Fo Hugoniot are: U_S = 6.41(24) + 1.03(2)u_P for the LPP region (fit to data in the range $0.71 \leq u_P \leq 1.28$ km/s corresponding to the stress range of 18 - 33 GPa); and U_S = 7.06(17) + 0.64(8)u_P for the MP region (fit to data in the range $1.37 \leq u_P \leq 2.86$ km/s corresponding to the stress range of 35 - 82 GPa) (see also Supplemental Material, Table S2).

The transition pressure to Fo III observed in the present work (~33 GPa) is lower than that observed in static studies (50 GPa for Fo II and 58 GPa for Fo III) (Finkelstein et al., 2014). This could partially be related to a sluggish reaction rate of the transition at room temperature (Zhang et al., 2019). Alternatively, large shear stresses under shock loading may play a role in driving the transition. A lowering of phase-transition pressure/stress in laser-based dynamic compression relative to static compression has been reported in other materials such as Si (McBride et al., 2019).

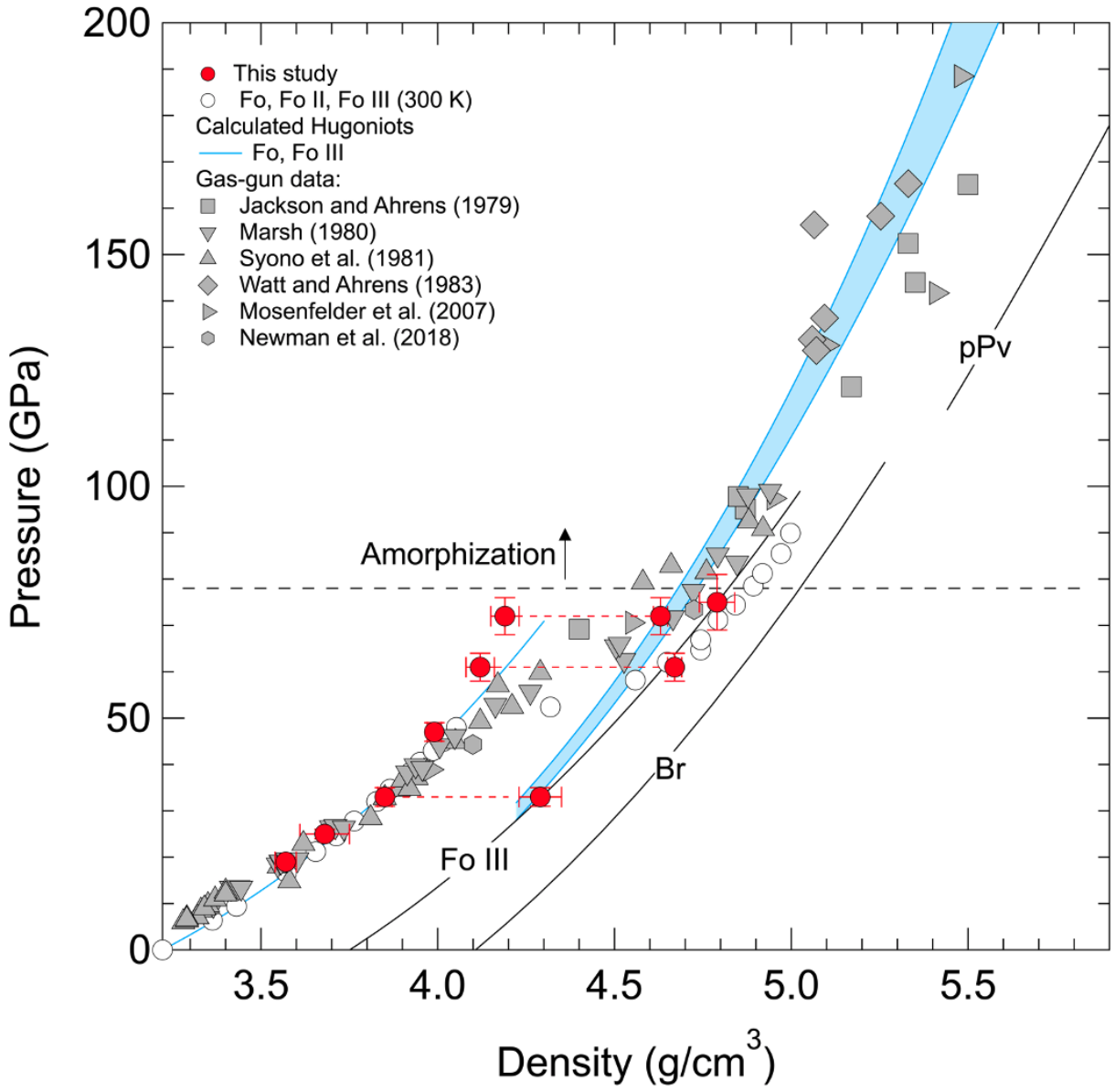

Figure 8. Densities determined from the present data (red symbols) compared to continuum gas-gun results (gray symbols) (Jackson & Ahrens, 1979; Marsh, 1980; Mosenfelder et al., 2007; Newman et al., 2018; Syono, Goto, Sato, et al., 1981; Watt & Ahrens, 1983). 300-K static compression data are shown as open symbols (Finkelstein et al., 2014). The light-blue solid line and shaded region indicate a calculated Hugoniot for forsterite and Fo III based on the thermodynamic parameters in the Supplemental Material, Table S6. The densities of the two components (Fo and Fo III) in the mixed-phase region are connected by red dashed lines. The Fo III (Zhang et al., 2019), bridgmanite (Br) (Tange et al., 2012) and post perovskite (pPv) (Sakai et al., 2016) pressure-volume EOS at 300 K are shown as solid curves.

447 4.3. Amorphization

448 Diffraction data from silicate glasses are generally characterized by a broad peak at low
449 Q [$Q = 4\pi \sin\theta/\lambda$, where λ equals wavelength] values, known as the first sharp diffraction
450 peak (FSDP). Under compression, a second feature (2nd sharp diffraction peak, SSDP) also
451 emerges in silicate glasses. Figure 9 shows the position of the first two sharp diffraction peaks
452 (SDPs) for amorphous Mg_2SiO_4 in our study compared to previous static and shock data for
453 Mg_2SiO_4 and $MgSiO_3$ glasses as a function of pressure. Our XRD data for shock-compressed
454 Mg_2SiO_4 show values and trends similar to the dynamic- and static-compression data for
455 $MgSiO_3$ glass (Supplemental Material, Table S5) (Morard et al., 2020) and static-compression
456 data for Mg_2SiO_4 glass (Benmore et al., 2011). The pressure dependence of the SDP positions
457 provides evidence of structural modifications under compression (Zeidler & Salmon, 2016). For
458 Mg_2SiO_4, the first SDP has been ascribed primarily to Mg-Mg and Mg-Si interactions, whereas
459 the second SDP is associated with O-O and Mg-O interactions appearing at high pressure
460 (Adjaoud et al., 2008; Benmore et al., 2011). The datasets for the two phases show a similar
461 trend with increasing pressure, indicating that the amorphous structures of Mg_2SiO_4 and $MgSiO_3$
462 materials may exhibit similar behavior in terms of atomic positions and packing.

463 Pressure-induced amorphization has been observed in many materials under static or
464 dynamic compression (Sharma & Sikka, 1996; Sikka & Gupta, 1998). Our results provide
465 evidence for shock-induced amorphization of forsterite above 79 GPa (Fig. 6). This contrasts
466 with previous interpretations of continuum gas-gun data that suggest decomposition to
467 crystalline periclase and bridgmanite (Mosenfelder et al., 2007; Syono, Goto, Takei, et al., 1981).
468 We do not observe any diffraction attributable to MgO in samples shocked to 122 GPa,
469 suggesting that crystallization of MgO is inhibited by the short timescales of these experiments.
470 In dynamic-compression experiments, transformation to an equilibrium or metastable crystalline
471 assemblage over laser (~ns) and/or gas-gun (~μs) timescales may be inhibited by low ionic
472 diffusivity in the solid state (Newman et al., 2018). As a result of this kinetic limitation, a
473 shocked sample may adopt a metastable amorphous structure as an intermediate state.

474 Pressure-induced amorphization in silicates is often driven by shear instabilities (Richet
475 & Gillet, 1997). The directional dependence of amorphization stress observed here may reflect
476 differences in shear stress along the Hugoniot at high compression. Interestingly, the
477 amorphization stress of Fo single crystals inversely correlates with their corresponding Hugoniot
478 Elastic Limit (HEL) values (and shear strength) as reported by Syono et al. (1981). The [010]
479 orientation, which has the highest HEL, exhibits more amorphization at lower stress than the
480 [100] orientation, which possesses the lowest HEL and does not amorphize up to 122 GPa. The
481 presence of stress anisotropy and different orientation relationships of the crystal with respect to
482 potential high-pressure polymorphs may lead to structural collapse at stresses that differ by
483 several tens of GPa for different orientations of Fo crystals.

484 It is well known that metals can retain at least some shear strength up until melting on the
485 Hugoniot and elastic anisotropy has been identified in aluminum single crystals shocked to 70
486 GPa (Choudhuri & Gupta, 2013). The degree of shear stress sustained by silicates under shock
487 loading is less clear. Measurements of sound speeds in some silicates are consistent with bulk
488 velocities and hence strengthless behavior (Dennis E. Grady et al., 1975). For shocked forsterite,
489 an orientation dependence of the Hugoniot density was reported above 100 GPa (Watt & Ahrens,
490 1983), but this was not confirmed in subsequent experiments (Michael D. Furnish & Brown,
491 1986). Sound-velocity measurements on shocked polycrystalline Fo and single-crystal olivine
492 from ~50-150 GPa suggest initial release-wave speeds consistent with longitudinal sound

493 velocities, and hence the retention of shear stiffness (J. M. Brown et al., 1987). Our results
494 further suggest that Fo may possess shear-stress anisotropy, leading to orientation-dependent
495 transformation behavior, as well as differences between single crystals and low-porosity
496 polycrystals that are retained up to 100 GPa or more.
497
498

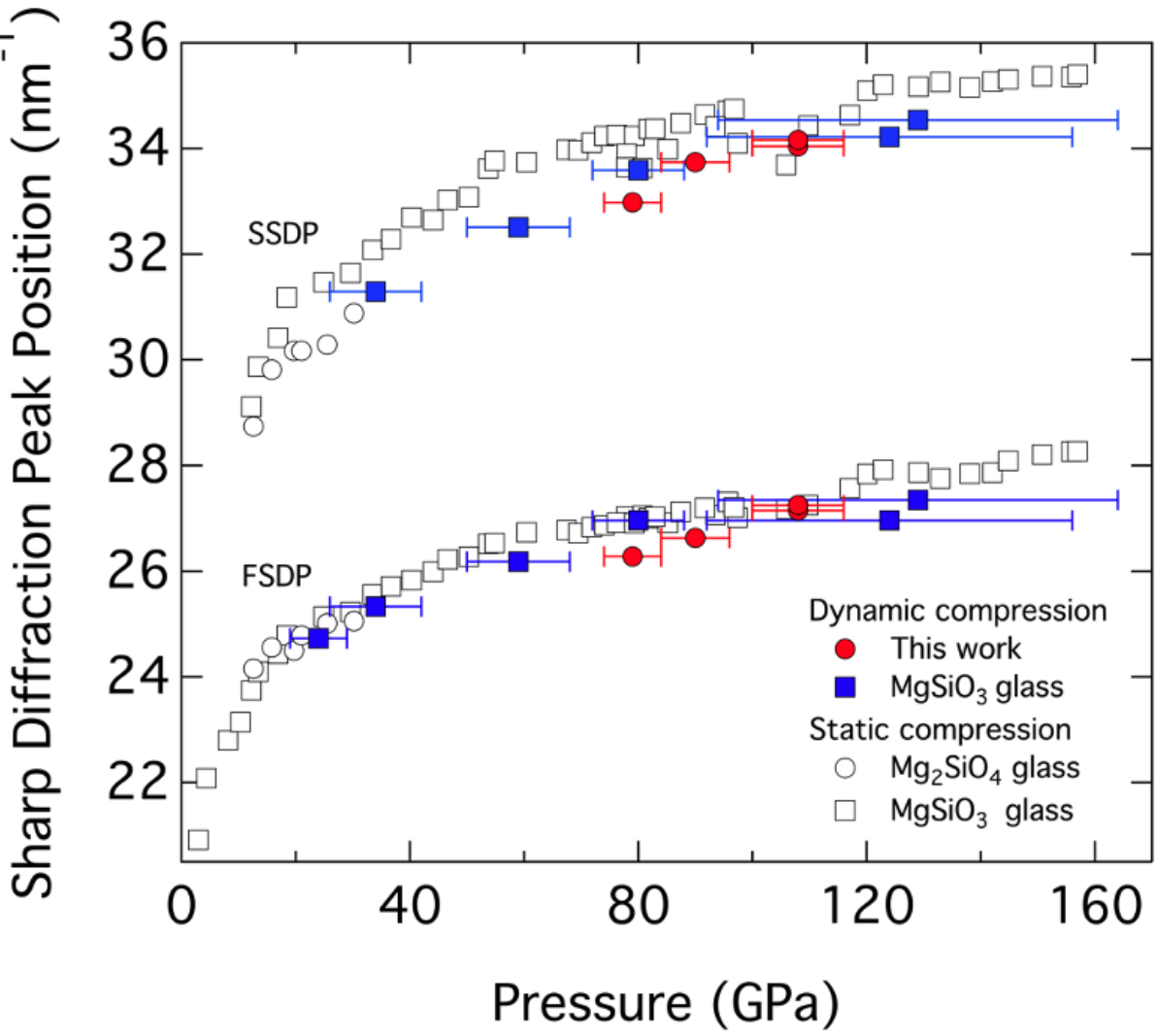

499
500
501 Figure 9. Position of the first (FSDP) and second (SSDP) sharp diffraction peaks for shocked-
502 compressed [010], [001] and polycrystalline forsterite (red circles) compared to laser-shock data
503 for $MgSiO_3$ (blue squares) (Morard et al., 2020) and static-compression data (open symbols) for
504 Mg_2SiO_4 (Benmore et al., 2011) and $MgSiO_3$ (Morard et al., 2020) glasses. For tabular data, see
505 the Supplemental Material, Table S5.
506
507
508
509
510

4.4. Stress Release at Late Time

X-ray diffraction patterns were recorded up to 63 ns after the start of stress release for select samples. We consistently observe persistence of, or recovery of, the forsterite structure after unloading (Figs. 3, 7 and S5). The diffraction patterns at these late times (~10-63 ns after shock breakout) have extended Debye-Scherrer rings compared to the shock-compressed states, indicating that the crystals have broken into or recrystallized as finer-grained crystallites showing a broader distribution of orientations. The unit-cell volumes obtained from our diffraction data upon release are larger than that of ambient forsterite by 2.0 %, 4.5 %, and 5.9% following peak stresses of 19, 33, and 122 GPa, respectively. This increase in volume may in part reflect residual high post-shock temperatures after adiabatic release.

The temperatures required to account for the observed late-time volumes following shock compression to the low stresses of 19 and 33 GPa in our experiments are about 880 and 1250 K, respectively, based on the thermal expansivity of forsterite (Kroll et al., 2012). These temperatures are significantly higher than the post-shock temperatures expected along the isentropic release paths (< 500 K) (Fig. 2), which should result in a volume expansion of less than 1 % at 1 bar. Recent molecular dynamic simulations and shock experiments (Heighway et al., 2019) have reported that the post-shock temperature of tantalum and rocks greatly exceeds values predicted by isentropic release. This difference is primarily explained by plastic-work heating with an additional contribution from heat released by the defects. Kurosawa and Genda (2018) has also suggested that additional heating on release in rocks with strength becomes significant using hydrodynamic simulations. Although the strength and nature of defects in Fo on shock loading and release are not known, we speculate that similar mechanisms may be operating in these silicate samples, contributing to the larger-than-expected observed released volumes.

Alternatively, we speculate that additional lattice expansion could arise from the small amounts of tension generated from the interaction of unloading waves. The spall strength determines the magnitude of tension that can be dynamically sustained. A uniform tensile stress of 1-3 GPa would be sufficient to explain the observed volumes for the low-stress shots (19 and 33 GPa), considering post-shock temperatures from isentropic release alone (Fig. 2). The spall strength of Fo is unknown, but available measurements on minerals and rocks yield values from 0.08-1.9 GPa (SiO_2 = 0.08-0.11 GPa, gabbro = 0.15 GPa, eclogite = 0.24 GPa, Al_2O_3 = 0.5-0.8 GPa, and ZrO_2 = 1.5-1.9 GPa) for strain rates of $\sim 10^4$ to 10^5 s^{-1} in gas-gun experiments (Ai & Ahrens, 2004; D E Grady, 1998). In general, the spall strength increases with increasing strain rate, but decreases with increasing shock-induced temperature (Kanel et al., 1996). Strain rates in laser-driven shock experiments (10^7- 10^9 s^{-1}) are 3 to 5 orders of magnitude higher than in plate-impact experiments, suggesting the spall strength of Fo may be higher than typical values measured in gas-gun experiments.

For the high-stress shot (122 GPa), the temperature required to explain the measured release volume (V = 307 Å^3) is about 1780 K. This is within the calculated temperature range (1590 – 1910 K) expected along the isentropic-release path from the peak stress of 122 GPa (Fig. 2), indicating good agreement between the measured volume and the expected release temperature. The higher temperature of these experiments may limit the material strength and thus reduce the contribution of plastic work heating or tensile stress on release. There is also evidence for possible amorphous or liquid Mg_2SiO_4 on release from this pressure (Fig. 7).

5. Conclusion

The atomic-level structure of forsterite was determined by X-ray diffraction under laser-driven shock loading to 19 – 122 GPa. Our results indicate that a mixture of forsterite and the metastable polymorph forsterite III coexists from ~33 to 75 GPa along the Hugoniot. This is generally consistent with a previous X-ray diffraction study using gas-gun experiments. The lattice parameters and densities for forsterite and forsterite III determined from our shock data are consistent with values from continuum gas-gun data, as well as static-compression and gas-gun X-ray diffraction studies. These results indicate that the transformation of forsterite to forsterite III can occur on timescales ranging from 10s of nanoseconds (laser compression) to ~microseconds (gas gun), as well as under low-temperature (300 K) static compression.

Higher stress behavior under dynamic loading depends on the initial crystal orientation. Polycrystalline forsterite undergoes amorphization above 79 GPa, but the [100]- and [001]-oriented single crystals show only partially disordered structures at 108 GPa. For the [100] orientation, an unknown crystalline phase occurs up to 122 GPa. For amorphous Mg_2SiO_4 at 79-108 GPa, two sharp diffraction peaks are observed. These exhibit behavior similar to amorphous Mg_2SiO_4 and $MgSiO_3$ under static compression and $MgSiO_3$ under dynamic compression, implying that the two materials may adopt similar dense structures under compression.

Upon release from high stress, we observe retention of or reversion to forsterite, with some evidence for the presence of amorphous material. The measured unit-cell volumes upon release from (peak stress) of 19 and 33 GPa are larger than the 300-K values. This difference may be explained by residual shock temperatures, plastic-work heating, and/or tensile stress. The unit-cell volume upon release from 122 GPa is consistent with the expected residual temperature due to isentropic release.

Overall, this study provides insight into the mechanisms and transformation pathways of forsterite under nanosecond-duration shock loading. Future experiments are needed to better understand the effects of timescale and loading rate on kinetics, metastability, and amorphization and thereby provide a better understanding of the behavior of this fundamental mineral across the timescales of laboratory and natural impact events.

Acknowledgements

The authors are grateful to Carol Davis of the target fabrication team at Lawrence Livermore National Laboratory (LLNL) and the staff at Matter in Extreme Conditions end-station for experimental assistance. A. M. Dillman and J. L. Mosenfelder synthesized the sintered polycrystalline samples. Gregory J. Finkelstein provided helpful comments on the manuscript. This research was supported by the U.S. Department of Energy (DE-SC0018925) and the National Science Foundation (NSF) (EAR-1644614). AEG acknowledges support from LANL Reines LDRD and the NSF Geophysics Program EAR-1446969. PDA acknowledges support from NSF Geophysics Program award EAR-1725349. MS and KA acknowledge support from the German Research Foundation DFG (AP 262/2-1 and FOR2440). This work was also performed under the auspices of the U.S Department of Energy by LLNL under contract No. DE-AC52-07NA27344. Use of the Linac Coherent Light Source , SLAC National Accelerator Laboratory, is supported by the Department of Energy, Office of Science, Office of Fusion Energy Sciences under Contract No. DE-AC02-76SF00515.

Additional experimental parameters and details of data extraction are available in the supporting information. Data from this work will be made available in the Department of Geosciences community of Princeton University's DataSpace.

References

Adjaoud, O., Steinle-Neumann, G., & Jahn, S. (2008). Mg_2SiO_4 liquid under high pressure from molecular dynamics. *Chemical Geology*, *256*(3–4), 185–192. https://doi.org/10.1016/j.chemgeo.2008.06.031

Ai, H.-A., & Ahrens, T. J. (2004). Dynamic tensile strength of terrestrial rocks and application to impact cratering. *Meteoritics & Planetary Science*, *39*(2), 233–246. https://doi.org/10.1111/j.1945-5100.2004.tb00338.x

Bauer, Jon. F. (1979). Experimental shock metamorphism of mono- and polycrystalline olivine: A comparative study. *Proceedings of the Lunar Planetary Science Conference*, *10th*, 2573–2596.

Benmore, C. J., Soignard, E., Guthrie, M., Amin, S. A., Weber, J. K. R., McKiernan, K., et al. (2011). High pressure x-ray diffraction measurements on Mg_2SiO_4 glass. *Journal of Non-Crystalline Solids*, *357*(14), 2632–2636. https://doi.org/10.1016/j.jnoncrysol.2010.12.064

van Boekel, R., Min, M., Leinert, Ch., Waters, L. B. F. M., Richichi, A., Chesneau, O., et al. (2004). The building blocks of planets within the 'terrestrial' region of protoplanetary disks. *Nature*, *432*(7016), 479–482. https://doi.org/10.1038/nature03088

Bouibes, A., & Zaoui, A. (2020). High-pressure phase transitions of forsterite from first-principles. *Journal of Physics and Chemistry of Solids*, *136*, 109161. https://doi.org/10.1016/j.jpcs.2019.109161

Brown, J. M., Furnish, M. D., & McQueen, R. G. (1987). Thermodynamics for $(Mg,Fe)_2SiO_4$ from the Hugoniot. In M. H. Manghnani & Y. Syono (Eds.), *Geophysical Monograph Series* (Vol. 39, pp. 373–384). Washington, D. C.: American Geophysical Union. https://doi.org/10.1029/GM039p0373

Brown, S. B., Hashim, A., Gleason, A., Galtier, E., Nam, I., Xing, Z., et al. (2017). Shock drive capabilities of a 30-Joule laser at the matter in extreme conditions hutch of the Linac Coherent Light Source. *Review of Scientific Instruments*, *88*(10), 105113. https://doi.org/10.1063/1.4997756

Choudhuri, D., & Gupta, Y. M. (2013). Shock compression of aluminum single crystals to 70 GPa: Role of crystalline anisotropy. *Journal of Applied Physics*, *114*(15), 153504. https://doi.org/10.1063/1.4824825

Errandonea, D. (2014). AB_2O_4 compounds at high pressures. In F. J. Manjon, I. Tiginyanu, & V. Ursaki (Eds.), *Pressure-Induced Phase Transitions in AB_2X_4 Chalcogenide Compounds* (Vol. 189, pp. 53–73). Berlin, Heidelberg: Springer Berlin Heidelberg. https://doi.org/10.1007/978-3-642-40367-5_2

Finkelstein, G. J., Dera, P. K., Jahn, S., Oganov, A. R., Holl, C. M., Meng, Y., & Duffy, T. S. (2014). Phase transitions and equation of state of forsterite to 90 GPa from single-crystal X-ray diffraction and molecular modeling. *American Mineralogist*, *99*(1), 35–43. https://doi.org/10.2138/am.2014.4526

Frost, D. J. (2008). The upper mantle and transition zone. *Elements*, *4*(3), 171–176. https://doi.org/10.2113/GSELEMENTS.4.3.171

Furnish, M. D., Grady, D. E., & Brown, J. M. (1986). Analysis of shock wave structure in single-crystal olivine using VISAR. In Y. M. Gupta (Ed.), *Shock Waves in Condensed Matter* (pp. 595–600). North Holland, New York.

Furnish, Michael D., & Brown, J. M. (1986). Shock loading of single-crystal olivine in the 100–200 GPa range. *Journal of Geophysical Research*, *91*(B5), 4723. https://doi.org/10.1029/JB091iB05p04723

Gillet, P., El Goresy, A., Beck, P., & Chen, M. (2007). High-pressure mineral assemblages in shocked meteorites and shocked terrestrial rocks: Mechanisms of phase transformations and constraints to pressure and temperature histories. In E. Ohtani, *Advances in High-Pressure Mineralogy* (pp. 57–82). Geological Society of America. https://doi.org/10.1130/2007.2421(05)

Grady, D E. (1998). Shock-wave compression of brittle solids. *Mechanics of Materials*, *29*, 181–203.

Grady, Dennis E., Murri, W. J., & De Carli, P. S. (1975). Hugoniot sound velocities and phase transformations in two silicates. *Journal of Geophysical Research*, *80*(35), 4857–4861. https://doi.org/10.1029/JB080i035p04857

Hanner, M. S. (1999). The Silicate Material in Comets. In K. Altwegg, P. Ehrenfreund, J. Geiss, & W. F. Huebner (Eds.), *Composition and Origin of Cometary Materials* (pp. 99–108). Dordrecht: Springer Netherlands. https://doi.org/10.1007/978-94-011-4211-3_10

Heighway, P. G., Sliwa, M., McGonegle, D., Wehrenberg, C., Bolme, C. A., Eggert, J., et al. (2019). Nonisentropic release of a shocked solid. *Physical Review Letters*, *123*(24), 245501. https://doi.org/10.1103/PhysRevLett.123.245501

Inoue, I., Inubushi, Y., Sato, T., Tono, K., Katayama, T., Kameshima, T., et al. (2016). Observation of femtosecond X-ray interactions with matter using an X-ray–X-ray pump–probe scheme. *Proceedings of the National Academy of Sciences*, *113*(6), 1492–1497. https://doi.org/10.1073/pnas.1516426113

Jackson, I., & Ahrens, T. J. (1979). Shock wave compression of single-crystal forsterite. *Journal of Geophysical Research*, *84*(B6), 3039. https://doi.org/10.1029/JB084iB06p03039

Jeanloz, R. (1980). Shock effects in olivine and implications for Hugoniot data. *Journal of Geophysical Research*, *85*(B6), 3163. https://doi.org/10.1029/JB085iB06p03163

Kanel, G. I., Razorenov, S. V., Bogatch, A., Utkin, A. V., Fortov, V. E., & Grady, D. E. (1996). Spall fracture properties of aluminum and magnesium at high temperatures. *Journal of Applied Physics*, *79*(11), 8310–8317. https://doi.org/10.1063/1.362542

Katsura, T., & Ito, E. (1989). The system Mg_2SiO_4-Fe_2SiO_4 at high pressures and temperatures: Precise determination of stabilities of olivine, modified spinel, and spinel. *Journal of Geophysical Research: Solid Earth*, *94*(B11), 15663–15670. https://doi.org/10.1029/JB094iB11p15663

de Koker, N. P., Stixrude, L., & Karki, B. B. (2008). Thermodynamics, structure, dynamics, and freezing of Mg_2SiO_4 liquid at high pressure. *Geochimica et Cosmochimica Acta*, *72*(5), 1427–1441. https://doi.org/10.1016/j.gca.2007.12.019

Kroll, H., Kirfel, A., Heinemann, R., & Barbier, B. (2012). Volume thermal expansion and related thermophysical parameters in the Mg, Fe olivine solid-solution series. *European Journal of Mineralogy*, *24*(6), 935–956. https://doi.org/10.1127/0935-1221/2012/0024-2235

692 Kurosawa, K., & Genda, H. (2018). Effects of friction and plastic deformation in shock-
693 comminuted damaged rocks on impact heating. *Geophysical Research Letters*, *45*(2),
694 620–626. https://doi.org/10.1002/2017GL076285
695 Langenhorst, F., Boustie, M., Migault, A., & Romain, J. P. (1999). Laser shock experiments with
696 nanoseconds pulses: a new tool for the reproduction of shock defects in olivine. *Earth*
697 *and Planetary Science Letters*, *173*(3), 333–342. https://doi.org/10.1016/S0012-
698 821X(99)00224-1
699 Langenhorst, Falko. (2002). Shock metamorphism of some minerals: Basic introduction and
700 microstructural observations. *Bulletin of the Czech Geological Survey*, *77*, 265–282.
701 Lavina, B. (2019). Crystalline forsterite to 160 GPa. *Goldschmidt Conference*.
702 Luo, S.-N., Akins, J. A., Ahrens, T. J., & Asimow, P. D. (2004). Shock-compressed $MgSiO_3$
703 glass, enstatite, olivine, and quartz: Optical emission, temperatures, and melting. *Journal*
704 *of Geophysical Research: Solid Earth*, *109*(B5). https://doi.org/10.1029/2003JB002860
705 Marsh, S. P. (1980). LASL Shock Hugoniot Data (Vol. 5). Berkeley, California: University of
706 California Press.
707 Mason, B. (1963). Olivine composition in chondrites. *Geochimica et Cosmochimica Acta*, *27*,
708 1011–1023.
709 McBride, E. E., Krygier, A., Ehnes, A., Galtier, E., Harmand, M., Konôpková, Z., et al. (2019).
710 Phase transition lowering in dynamically compressed silicon. *Nature Physics*, *15*(1), 89–
711 94. https://doi.org/10.1038/s41567-018-0290-x
712 Medvedev, N., Tkachenko, V., Lipp, V., Li, Z., & Ziaja, B. (2018). Various damage mechanisms
713 in carbon and silicon materials under femtosecond X-ray irradiation. *4open*, *1*, 3.
714 https://doi.org/10.1051/fopen/2018003
715 Morard, G., Hernandez, J.-A., Guarguaglini, M., Bolis, R., Benuzzi-Mounaix, A., Vinci, T., et al.
716 (2020). In situ X-ray diffraction of silicate liquids and glasses under dynamic and static
717 compression to megabar pressures. *Proceedings of the National Academy of Sciences*.
718 https://doi.org/10.1073/pnas.1920470117
719 Mosenfelder, J. L., Asimow, P. D., & Ahrens, T. J. (2007). Thermodynamic properties of
720 Mg_2SiO_4 liquid at ultra-high pressures from shock measurements to 200 GPa on forsterite
721 and wadsleyite. *Journal of Geophysical Research*, *112*(B6), B06208.
722 https://doi.org/10.1029/2006JB004364
723 Müller, W. F., & Hornemann, U. (1969). Shock-induced planar deformation structures in
724 experimentally shock-loaded olivines and in olivines from chondritic meteorites. *Earth*
725 *and Planetary Science Letters*, *7*(3), 251–264. https://doi.org/10.1016/0012-
726 821X(69)90062-4
727 Mustard, J. F., Poulet, F., Gendrin, A., Bibring, J.-P., Langevin, Y., Gondet, B., et al. (2005).
728 Olivine and pyroxene diversity in the crust of Mars. *Science*, *307*(5715), 1594–1597.
729 https://doi.org/10.1126/science.1109098
730 Nagler, B., Arnold, B., Bouchard, G., Boyce, R. F., Boyce, R. M., Callen, A., et al. (2015). The
731 matter in extreme conditions instrument at the Linac Coherent Light Source. *Journal of*
732 *Synchrotron Radiation*, *22*(3), 520–525. https://doi.org/10.1107/S1600577515004865
733 Newman, M. G., Kraus, R. G., Akin, M. C., Bernier, J. V., Dillman, A. M., Homel, M. A., et al.
734 (2018). In situ observations of phase changes in shock compressed forsterite.
735 *Geophysical Research Letters*, *45*(16), 8129–8135.
736 https://doi.org/10.1029/2018GL077996

Nguyen, A. N. (2004). Discovery of ancient silicate stardust in a meteorite. *Science*, *303*(5663), 1496–1499. https://doi.org/10.1126/science.1094389

Oganov, A. R., & Ono, S. (2004). Theoretical and experimental evidence for a post-perovskite phase of $MgSiO_3$ in Earth's D″ layer. *Nature*, *430*, 445–448. https://doi.org/10.1038/nature02701

Philipp, H. T., Hromalik, M., Tate, M., Koerner, L., & Gruner, S. M. (2011). Pixel array detector for X-ray free electron laser experiments. *Nuclear Instruments and Methods in Physics Research Section A: Accelerators, Spectrometers, Detectors and Associated Equipment*, *649*(1), 67–69. https://doi.org/10.1016/j.nima.2010.11.189

Prescher, C., & Prakapenka, V. B. (2015). *DIOPTAS* : a program for reduction of two-dimensional X-ray diffraction data and data exploration. *High Pressure Research*, *35*(3), 223–230. https://doi.org/10.1080/08957959.2015.1059835

Reimold, W. U., & Stöffler, D. (1978). Experimental shock metamorphism of dunite. *Proc. Lunar Plnaet. Sci. Conf.*, *9th*, 2805–2824.

Richet, P., & Gillet, P. (1997). Pressure-induced amorphization of minerals: a review. *European Journal of Mineralogy*, *9*(5), 907–934. https://doi.org/10.1127/ejm/9/5/0907

Ringwood, A. E. (1991). Phase transformations and their bearing on the constitution and dynamics of the mantle. *Geochimica et Cosmochimica Acta*, *55*(8), 2083–2110. https://doi.org/10.1016/0016-7037(91)90090-R

Sakai, T., Dekura, H., & Hirao, N. (2016). Experimental and theoretical thermal equations of state of $MgSiO_3$ post-perovskite at multi-megabar pressures. *Scientific Reports*, *6*(1), 22652. https://doi.org/10.1038/srep22652

Sharma, S. M., & Sikka, S. K. (1996). Pressure induced amorphization of materials. *Progress in Materials Science*, *40*(1), 1–77. https://doi.org/10.1016/0079-6425(95)00006-2

Shinno, I. (2002). A Raman spectroscopic study of shocked forsterite. *Journal of Mineralogical and Petrological Sciences*, *97*(4), 153–160. https://doi.org/10.2465/jmps.97.153

Sikka, S. K., & Gupta, S. C. (1998). Shock induced amorphization of materials. *AIP Conference Proceedings*, *429*, 145–150.

Smith, R. F., Eggert, J. H., Rudd, R. E., Swift, D. C., Bolme, C. A., & Collins, G. W. (2011). High strain-rate plastic flow in Al and Fe. *Journal of Applied Physics*, *110*(12), 123515. https://doi.org/10.1063/1.3670001

Smyth, J. R., Jacobsen, S. D., & Hazen, R. M. (2000a). Comparative crystal chemistry of dense oxide minerals. *Reviews in Mineralogy and Geochemistry*, *41*(1), 157–186. https://doi.org/10.2138/rmg.2000.41.6

Smyth, J. R., Jacobsen, S. D., & Hazen, R. M. (2000b). Comparative crystal chemistry of orthosilicate minerals. *Reviews in Mineralogy and Geochemistry*, *41*(1), 187–209. https://doi.org/10.2138/rmg.2000.41.7

Stacey, F. D., & Davis, P. M. (2008). *Physics of the Earth* (4th ed.). Cambridge: Cambridge Univ. Press.

Syono, Y., Goto, T., Takei, H., Tokonami, M., & Nobugai, K. (1981). Association reaction in forsterite under shock compression. *Science*, *214*(4517), 177. https://doi.org/10.1126/science.214.4517.177

Syono, Y., Goto, T., Sato, J., & Takei, H. (1981). Shock compression measurements of single-crystal forsterite in the pressure range 15-93 GPa. *Journal of Geophysical Research: Solid Earth*, *86*(B7), 6181–6186. https://doi.org/10.1029/JB086iB07p06181

Tange, Y., Kuwayama, Y., Irifune, T., Funakoshi, K., & Ohishi, Y. (2012). P-V-T equation of state of $MgSiO_3$ perovskite based on the MgO pressure scale: A comprehensive reference for mineralogy of the lower mantle. *Journal of Geophysical Research: Solid Earth*, *117*(B6), B06201. https://doi.org/10.1029/2011JB008988

Tateno, S., Hirose, K., Ohishi, Y., & Tatsumi, Y. (2010). The structure of iron in Earth's inner core. *Science*, *330*(6002), 359–361. https://doi.org/10.1126/science.1194662

Tracy, S. J., Smith, R. F., Wicks, J. K., Fratanduono, D. E., Gleason, A. E., Bolme, C. A., et al. (2019). In situ observation of a phase transition in silicon carbide under shock compression using pulsed x-ray diffraction. *Physical Review B*, *99*(21), 214106. https://doi.org/10.1103/PhysRevB.99.214106

Watt, J. P., & Ahrens, T. J. (1983). Shock compression of single-crystal forsterite. *Journal of Geophysical Research: Solid Earth*, *88*(B11), 9500–9512. https://doi.org/10.1029/JB088iB11p09500

Wilding, M. C., Benmore, C. J., & Weber, J. K. R. (2008). In situ diffraction studies of magnesium silicate liquids. *Journal of Materials Science*, *43*(14), 4707–4713. https://doi.org/10.1007/s10853-007-2356-5

Yamanaka, T., Uchida, A., & Nakamoto, Y. (2008). Structural transition of post-spinel phases $CaMn_2O_4$, $CaFe_2O_4$, and $CaTi_2O_4$ under high pressures up to 80 GPa. *American Mineralogist*, *93*(11–12), 1874–1881. https://doi.org/10.2138/am.2008.2934

Zeidler, A., & Salmon, P. S. (2016). Pressure-driven transformation of the ordering in amorphous network-forming materials. *Physical Review B*, *93*(21), 214204. https://doi.org/10.1103/PhysRevB.93.214204

Zerr, A. (1998). Solidus of Earth's deep mantle. *Science*, *281*(5374), 243–246. https://doi.org/10.1126/science.281.5374.243

Zhang, Y., Zhang, Y., Liu, Y., & Liu, X. (2019). A metastable Fo-III wedge in cold slabs subducted to the lower part of the mantle transition zone: A hypothesis based on first-principles simulations. *Minerals*, *9*(3), 186. https://doi.org/10.3390/min9030186